digital

MDPI

Article

Comparative Assessment of Machine Learning and Neural Network Models for Asbestos–Cement Detection in VNIR Images

Gabriel Elías Chanchí-Golondrino [1], Isaac Esteban Camargo Freile [2], Julio Eduardo Mejía Manzano [2], Manuel Saba [1,*] and Manuel Alejandro Ospina-Alarcón [1]

[1] Facultad de Ingeniería, Universidad de Cartagena, Colombia Cll. 30 #39 B-192, Piedra de Bolívar, Ave. del Consulado, Cartagena 130015, Colombia; gchanchig@unicartagena.edu.co (G.E.C.-G.); mospinaa@unicartagena.edu.co (M.A.O.-A.)

[2] Escuela de Ciencias Básicas, Tecnología e Ingeniería, Universidad Nacional Abierta y a Distancia (UNAD), Cll 14 Sur # 14 - 23, Bogotá 111411, Colombia; isaac.camargo@unad.edu.co (I.E.C.F.); julioe.mejia@unad.edu.co (J.E.M.M.)

* Correspondence: msaba@unicartagena.edu.co

Abstract

Hyperspectral imaging is a well-established remote sensing technique for material detection and classification, relying on hundreds of reflectance bands to exploit the spectral signatures of surface materials. Although hyperspectral imagery has demonstrated excellent capabilities for material identification, its operational implementation may be constrained in some applications due to data volume and processing requirements. Consequently, there is growing interest in evaluating the capability of lower-dimensional multispectral imagery for material detection tasks. In this sense, this article proposes as its contribution the comparative evaluation of machine learning models and neural networks for asbestos–cement detection on VNIR imagery. For the development of this research, the CRISP-DM methodology was adapted into four phases: P1. Business and data understanding; P2. Data preparation; P3. Modelling and evaluation; P4. Model deployment. At the results level, three datasets with different numbers of bands were constructed, which were structured by adding to the original dataset an additional layer with the NDVI and two additional layers with the PCA components of the original image. Across the three datasets, four machine learning models and one neural network model were tuned and evaluated, yielding as a result that in all three datasets the KNN and neural network models achieved the best performance. Likewise, it was found that the detection capability of the models improved with the inclusion of the additional bands. The proposed approach serves as a reference to be extrapolated by research centres and universities for the detection of asbestos and other materials in VNIR images, with a view toward integration into resource-constrained systems and specifically into environmental monitoring systems.

Keywords: asbestos–cement; NIR imagery; machine learning; neural networks; remote sensing

Check for updates

Academic Editor: Manuel Reis

Received: 1 June 2026
Revised: 17 July 2026
Accepted: 23 July 2026
Published: 27 July 2026

Copyright: © 2026 by the authors. Licensee MDPI, Basel, Switzerland. This article is an open access article distributed under the terms and conditions of the Creative Commons Attribution (CC BY) license.

1. Introduction

Remote sensing can be defined as a technology that enables the acquisition of information about objects on the Earth's surface without direct physical contact. This is achieved through sensors mounted on satellites, aircraft, or unmanned aerial vehicles (UAVs), which

capture the electromagnetic radiation reflected or emitted by surface materials, thereby enabling the identification, measurement, and analysis of their characteristics [1–5]. Compared with conventional field-based methods, remote sensing facilitates the non-invasive monitoring of extensive geographical areas and the efficient acquisition of large volumes of data, enabling continuous assessment of environmental and surface changes through periodically acquired imagery [6–8].

Among the various remote sensing techniques, hyperspectral imaging has emerged as one of the most widely adopted and powerful approaches. Hyperspectral imaging can be defined as an advanced image acquisition technique that integrates spectroscopy with conventional imaging, generating a three-dimensional data cube composed of two spatial dimensions (x, y) and one spectral dimension (λ). In this structure, each pixel contains a complete spectral signature representing the reflected, transmitted, or emitted radiation of the observed object across a continuous range of wavelengths, typically extending from the ultraviolet to the mid-infrared region of the electromagnetic spectrum [9–11]. By capturing information across hundreds of narrow and contiguous spectral bands, each corresponding to a specific wavelength, hyperspectral imaging enables the detailed characterization of the geometric, physical, and chemical properties of materials, providing valuable information for their identification and classification [12,13].

Despite their significant analytical capabilities, hyperspectral images contain hundreds of spectral bands, which introduces several challenges related to data volume and spectral redundancy. These characteristics substantially increase memory and computational requirements, limiting real-time analysis and hindering the deployment of hyperspectral systems in resource-constrained environments [14–16]. Furthermore, the storage and management of hyperspectral data cubes are often associated with considerable computational costs. As a result, dimensionality reduction and data compression techniques, such as Principal Component Analysis (PCA), are frequently employed to mitigate these limitations. However, these methods can themselves be computationally demanding, particularly during the processing of large covariance matrices and the reconstruction of compressed datasets [17–19]. Although hyperspectral imagery generally provides superior material discrimination capabilities due to its rich spectral information, multispectral imagery has also demonstrated considerable potential for material detection tasks in environmental monitoring applications [20–22].

Numerous studies have explored the use of spectral imagery for the detection and mapping of asbestos-containing materials. In Italy, SWIR hyperspectral imagery combined with chemometric analysis was employed to classify amosite, chrysotile, and crocidolite fibres, achieving sensitivity and specificity values ranging from 0.89 to 1.00 [23,24]. Similarly, multispectral imagery acquired by the WorldView-3 satellite, together with supervised Maximum Likelihood classifiers, was used to detect asbestos–cement roofing in Mantua, Italy, yielding an overall accuracy of 87% [25]. In Israel, satellite hyperspectral data acquired by the EnMAP sensor were combined with multiple supervised classification algorithms to map asbestos–cement roofs in complex urban environments, achieving a positive matching rate of 86% [26]. In the United States, airborne hyperspectral imagery was applied to monitor restoration processes at an asbestos mine, enabling the discrimination of treated and untreated areas with an overall accuracy of 84%, which increased to 96% after the exclusion of selected variables from the analysis [27]. Likewise, in Australia, high-resolution multispectral and aerial imagery were integrated with convolutional neural networks based on the Mask R-CNN architecture to identify roofs containing asbestos materials, reaching an accuracy of 94% [28]. Finally, in Poland, convolutional neural networks were employed to detect asbestos–cement roofing from RGB and infrared aerial photographs, achieving overall accuracies ranging from 87% to 89% [29].

The studies discussed above demonstrate the effectiveness of spectral imagery for asbestos–cement detection. Considering the growing interest in low-dimensional remote sensing approaches for operational environmental monitoring, this study presents a comparative evaluation of machine learning algorithms and sequential neural network models for the detection of asbestos–cement materials using four-band visible near-infrared (VNIR) multispectral imagery.

As a key contribution, the proposed framework extends beyond the evaluation of a conventional four-band dataset by assessing model performance on two additional datasets containing five and seven features, respectively. The five-band dataset incorporates an additional layer corresponding to the Normalized Difference Vegetation Index (NDVI), whereas the seven-band dataset further includes the NDVI layer together with two additional features derived from the first two principal components obtained through Principal Component Analysis (PCA) of the original imagery. This multi-dataset approach enables a systematic assessment of the impact of feature augmentation and dimensionality reduction techniques on classification performance.

The scientific contribution of this study includes the evaluation of asbestos–cement detection using very high spatial resolution four-band VNIR imagery supported by field-verified reference samples; the comparative assessment of lightweight machine learning models, including neural networks, under multiple feature-space configurations; and the analysis of the contribution of NDVI and PCA-derived features to classification performance; and the demonstration of the potential of low-dimensional multispectral imagery for operational asbestos–cement monitoring applications. The remainder of this paper is organized as follows. Section 2 presents the methodological framework, including the adaptation and implementation of the Cross-Industry Standard Process for Data Mining (CRISP-DM) methodology. Section 3 describes the datasets considered in this study and discusses the results obtained from the training and evaluation of the machine learning and artificial neural network models. Finally, Section 4 summarizes the main conclusions and outlines future research directions arising from this work.

2. Materials and Methods

To conduct the present study, the CRISP-DM methodology was adapted into a four-phase framework comprising: P1. Business and Data Understanding, P2. Data Preparation, P3. Modelling and Evaluation, and P4. Deployment (see Figure 1). The CRISP-DM methodology was selected because of its flexibility and applicability across diverse domains, as well as its well-established and structured framework for data-driven research. In particular, it facilitates the systematic definition of project objectives, supports data quality management, and ensures the traceability of decisions throughout the entire project lifecycle. These characteristics make CRISP-DM especially suitable for machine learning studies involving complex datasets and iterative model development processes [30–33].

During Phase 1 of the methodology, a set of sample points representing asbestos–cement and non-asbestos materials was selected from a four-band visible near-infrared (VNIR) aerial image with a spatial resolution of 0.17 m per pixel, covering the Manga neighbourhood in Cartagena, Colombia. Sample selection was performed using the open-source software ImageJ (version 1.54g, National Institutes of Health, Bethesda, MD, USA), which enables the extraction of pixel coordinates from user-defined regions of interest. Using this procedure, a total of 2000 sample pixels were identified, comprising 1000 asbestos–cement pixels and 1000 pixels corresponding to other surface materials. These samples are represented by blue and red markers, respectively, in the reference image shown in Figure 2. It is worth mentioning that the random asbestos cement samples were selected from a large roof whose composition had been previously verified through field visits,

thereby ensuring the correct identification of the material. Furthermore, this roof exhibits heterogeneities associated with factors such as ageing, preservation condition, and surface characteristics, which made it possible to capture representative variability in the spectral response. Although these variations may modify the magnitude of reflectance, they do not alter the characteristic shape of the spectral signature, which is primarily determined by the physicochemical properties of the material. Consequently, the selected samples were considered to provide an adequate representation of the spectral response of asbestos cement for its differentiation from other materials present in the scene. It is worth mentioning that the 1000 spectral signatures corresponding to other materials were obtained through visual inspection using the open-source ImageJ tool, which was employed to identify and record the pixel coordinates of representative regions containing materials such as water bodies, vegetation, and paved roads. Based on these coordinates, random sampling was performed using a fixed random seed through the Python pandas library version 3.12.13.

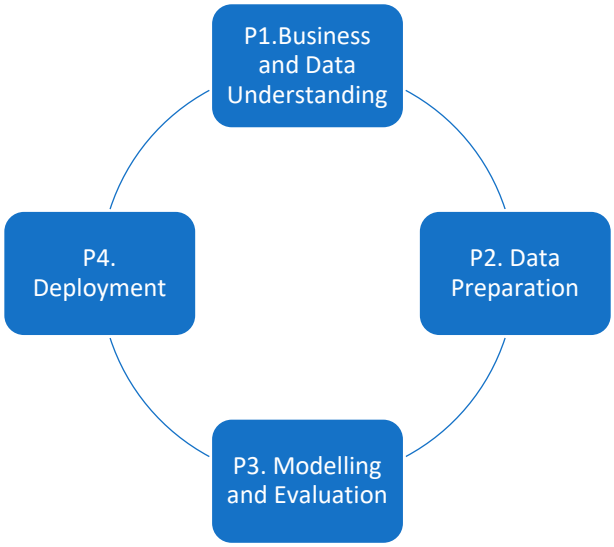


Figure 1. Methodology workflow.

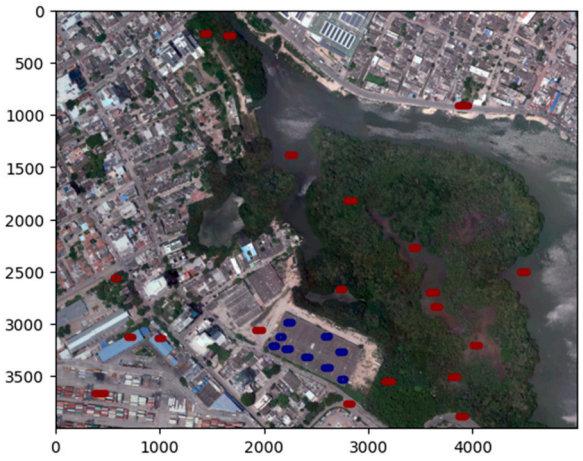


Figure 2. Sample points selected from the reference image.

It is important to note that each sample point shown in Figure 2 is associated with a spectral signature composed of four features corresponding to the pixel values of the RGB bands and the reflectance value of the near-infrared (NIR) band. Based on these data, Figure 3 presents the spectral signatures of a representative subset consisting of 100 asbestos–cement samples and 100 samples corresponding to other materials. Only this representative subset is shown to improve figure readability.

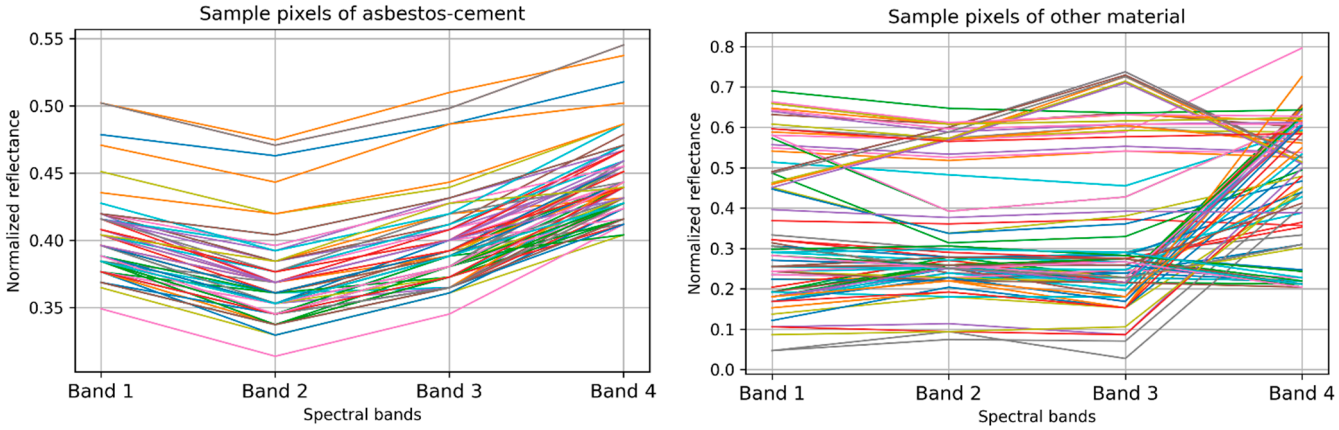


Figure 3. Spectral signatures of a representative subset (100 samples per class) extracted from the asbestos–cement and other-material datasets.

In Phase 2 of the methodology, a labelled base dataset was first constructed using the extracted sample spectral signatures. For classification purposes, asbestos–cement samples were assigned the label 1, whereas samples corresponding to other materials were assigned the label 0. The resulting dataset, represented as a dataframe, is illustrated in Figure 4.

	band1	band2	band3	band4	pixel
0	0.384314	0.345098	0.392157	0.431373	1.0
1	0.415686	0.392157	0.419608	0.458824	1.0
2	0.376471	0.337255	0.364706	0.423529	1.0
3	0.415686	0.376471	0.411765	0.454902	1.0
4	0.368627	0.337255	0.360784	0.423529	1.0
...	...	...	...	...	...
1995	0.321569	0.290196	0.274510	0.352941	0.0
1996	0.168627	0.239216	0.207843	0.592157	0.0
1997	0.490196	0.588235	0.729412	0.525490	0.0
1998	0.662745	0.611765	0.631373	0.627451	0.0
1999	0.243137	0.227451	0.215686	0.211765	0.0

2000 rows × 5 columns

Figure 4. Labelled spectral signature dataset.

The dataset was generated using functionalities provided by the Python NumPy library, which enabled the concatenation of the two groups of spectral signatures into a single matrix containing 2000 observations. An additional column was subsequently appended to store the class labels associated with each sample pixel, thereby creating the final labelled dataset used for model training and evaluation.

The dataset presented in Figure 4 consists of a total of 2000 instances, including 1000 asbestos–cement samples and 1000 samples corresponding to other materials. The base dataset contains five columns: normalized reflectance values corresponding to the RGB and near-infrared (NIR) bands for each pixel, together with the class label assigned to each sample. Additionally, two new datasets containing five and seven spectral features,

respectively, were derived from the original four-band dataset. The five-feature dataset incorporates an additional variable corresponding to the Normalized Difference Vegetation Index (NDVI), whereas the seven-feature dataset further includes two additional variables representing the first two principal components obtained through Principal Component Analysis (PCA). These augmented datasets were generated to evaluate the fitting and classification capabilities of the considered classical machine learning algorithms and the proposed artificial neural network model under different feature-space configurations.

It should be noted that the *NDVI* is one of the most widely used spectral indices for characterizing vegetation and can be mathematically expressed according to Equation (1).

$$NDVI = \frac{NIR - Red}{NIR + Red} \tag{1}$$

In Equation (1), *NIR* corresponds to the pixel value of the fourth band of the image, representing the near-infrared spectral region, whereas Red corresponds to the first spectral band of the image. The NDVI was selected as an additional feature because it effectively enhances spectral differences between vegetated and non-vegetated surfaces through the combination of the red and near-infrared bands. Consequently, this index provides complementary information beyond that contained in the original image bands and may help reduce confusion between asbestos–cement roofs and surrounding vegetated areas within heterogeneous urban environments. However, NDVI is not a specific indicator of asbestos–cement materials and is not expected to directly discriminate asbestos–cement roofs from spectrally similar urban surfaces such as concrete, road pavements, bare soil, or other roofing materials. The incorporation of this additional information, therefore, aims to complement, rather than replace, the discriminatory capability provided by the original spectral bands.

Regarding Principal Component Analysis (PCA), let a four-band NIR multispectral image be represented as ($X = [R, G, B, NIR]$). The objective of PCA is to transform the original feature space into a new representation, denoted as ($X_{PCA} = [PC_1 \dots PC_N]$), with reduced dimensionality while preserving as much of the original data variance as possible. This transformation generates a set of orthogonal principal components that capture the dominant patterns of variability present in the image. Each principal component can be expressed according to Equation (2), where the coefficients a_i, b_i, c_i, and d_i represent the weights associated with the original spectral bands. These coefficients determine the contribution of each band to the corresponding principal component and are computed to maximize the explained variance under the orthogonality constraints imposed by the PCA transformation.

$$PC_i = a_i R + b_i G + c_i B + d_i NIR \tag{2}$$

In Phase 3 of the methodology, the training and performance evaluation of four machine learning algorithms (Decision Trees, K Nearest Neighbours (KNN), Support Vector Machines (SVM), and Logistic Regression) together with a Sequential Artificial Neural Network (ANN) model were carried out using each of the three datasets developed in Phase 2. For each dataset, the samples were partitioned at the pixel level into training and testing sets using an 80/20 stratified split with a fixed random seed, ensuring that the class proportions were preserved in both partitions. The objective was to assess the classification capability of both conventional machine learning approaches and deep learning techniques under different feature-space configurations. Model performance was evaluated using standard metrics derived from the confusion matrix, including Accuracy, Precision, Recall, and F1-score. These metrics enabled a comprehensive comparative analysis of the different classification models across the three datasets, namely the original four-band dataset, the

dataset incorporating the NDVI feature, and the dataset augmented with both NDVI and PCA-derived components.

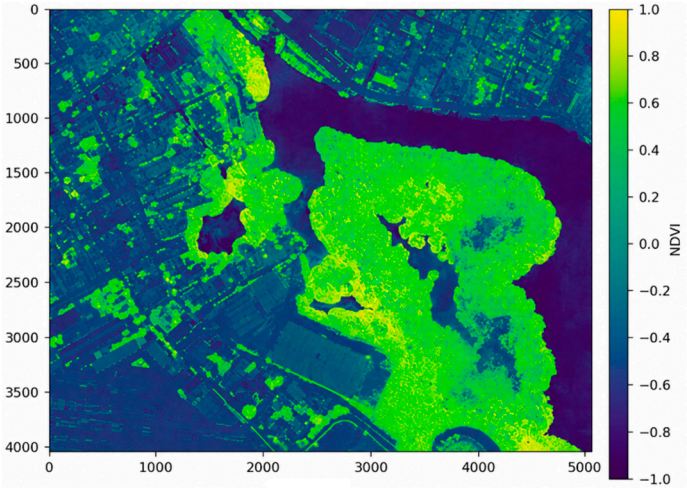
Finally, in Phase 4, the trained and validated models were deployed over the entire multispectral NIR image to perform pixel-wise asbestos–cement detection. This process enabled the estimation of the percentage of pixels classified as asbestos–cement by each model, as well as the visual identification of the spatial distribution of the detected asbestos-containing areas. To facilitate qualitative comparison, a grid of classification maps was generated, allowing visual assessment of model predictions across the three feature configurations considered in this study. This approach enabled the evaluation of the influence of NDVI and PCA-derived features on the spatial detection patterns and overall classification performance of the proposed models.

3. Results and Discussion

3.1. Data Preparation and Feature Engineering

In the results stage, the first step consisted of calculating the Normalized Difference Vegetation Index (NDVI), a spectral index derived from the red (R) and near-infrared (NIR) bands that is widely used to enhance the distinction between vegetated and non-vegetated surfaces. In the context of asbestos–cement detection, the NDVI provides complementary information because asbestos–cement roofs typically exhibit spectral responses characteristic of non-vegetated surfaces, similar to those observed in bare soils and exposed built structures.

Consequently, the incorporation of NDVI facilitates the differentiation of asbestos–cement roofs from densely vegetated areas and other surrounding land-cover types, thereby reducing the likelihood of false-positive detections and improving the overall classification process in multispectral imagery. Furthermore, the inclusion of this spectral index introduces additional discriminatory information that may enhance the predictive performance of the evaluated classification models. Figure 5 presents the NDVI layer generated from the original multispectral image, together with the second dataset derived from the base dataset through the incorporation of the NDVI feature as an additional predictor variable. The colour scale represents NDVI values ranging from −1 to 1, where lower values correspond to water or non-vegetated surfaces and higher values indicate denser vegetation.



	band1	band2	band3	band4	band5	pixel
0	0.384314	0.345098	0.392157	0.431373	0.528846	1.0
1	0.415686	0.392157	0.419608	0.458824	0.524664	1.0
2	0.376471	0.337255	0.364706	0.423529	0.529412	1.0
3	0.415686	0.376471	0.411765	0.454902	0.522523	1.0
4	0.368627	0.337255	0.360784	0.423529	0.534653	1.0
...	...	...	...	...	...	...
1995	0.321569	0.290196	0.274510	0.352941	0.523256	0.0
1996	0.168627	0.239216	0.207843	0.592157	0.778351	0.0
1997	0.490196	0.588235	0.729412	0.525490	0.517375	0.0
1998	0.662745	0.611765	0.631373	0.627451	0.486322	0.0
1999	0.243137	0.227451	0.215686	0.211765	0.465517	0.0

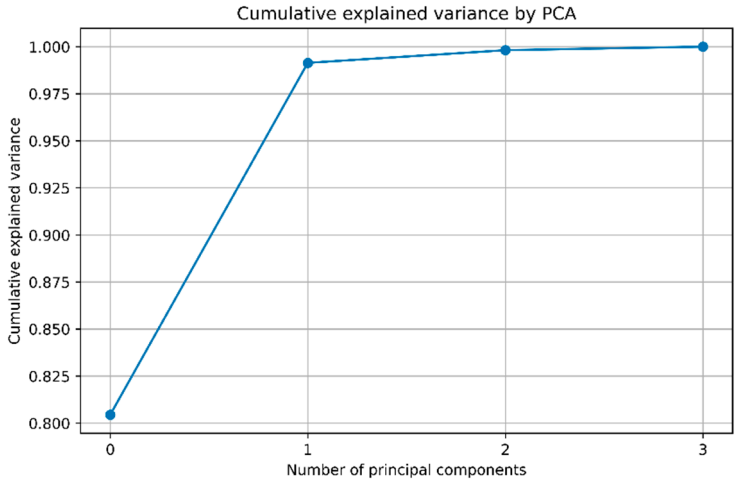
2000 rows × 6 columns

Figure 5. Generated NDVI layer and resulting five-feature dataset. The colour scale represents NDVI values ranging from low vegetation density (dark colours) to high vegetation density (bright colours).

As shown in Figure 5, the feature referred to as Band 5 corresponds to the NDVI layer computed from the NIR band (Band 4) and the red band (Band 1) of the original

multispectral image. The incorporation of this spectral index extends the original feature space by providing complementary information related to vegetation discrimination.

Subsequently, a third dataset was generated by augmenting the original five-feature dataset with two additional variables corresponding to the first two principal components obtained from the PCA transformation of the original four-band NIR image. The first principal component (PC1) explains approximately 80% of the total variance, while the second principal component (PC2) increases the cumulative explained variance to approximately 99%, indicating that these two components capture nearly all the spectral information contained in the original dataset. Figure 6 presents the cumulative explained variance associated with the principal components and the resulting seven-feature dataset. In this dataset, Bands 6 and 7 correspond to PC1 and PC2, respectively, and were incorporated as additional predictor variables for the subsequent classification experiments. Therefore, in this study, PCA was employed as a feature augmentation technique rather than as a dimensionality reduction method, since the original spectral bands and the NDVI were preserved, and the principal components were incorporated as complementary features.



	band1	band2	band3	band4	band5	band6	band7	pixel
0	0.384314	0.345098	0.392157	0.431373	0.528846	0.367949	0.331701	1.0
1	0.415686	0.392157	0.419608	0.458824	0.524664	0.402808	0.339208	1.0
2	0.376471	0.337255	0.364706	0.423529	0.529412	0.353936	0.331535	1.0
3	0.415686	0.376471	0.411765	0.454902	0.522523	0.395431	0.338551	1.0
4	0.368627	0.337255	0.360784	0.423529	0.534653	0.350340	0.332507	1.0
...	...	...	...	...	...	...	...	...
1995	0.321569	0.290196	0.274510	0.352941	0.523256	0.287342	0.310480	0.0
1996	0.168627	0.239216	0.207843	0.592157	0.778351	0.235280	0.453235	0.0
1997	0.490196	0.588235	0.729412	0.525490	0.517375	0.584774	0.327491	0.0
1998	0.662745	0.611765	0.631373	0.627451	0.486322	0.626850	0.378888	0.0
1999	0.243137	0.227451	0.215686	0.211765	0.465517	0.209921	0.251518	0.0

2000 rows × 8 columns

Figure 6. PCA and 7-layer conformal dataset.

3.2. Modelling and Evaluation

After constructing the three experimental datasets, the four machine learning models (DT, SVM, LR, and KNN) were trained and evaluated using the 4-band, 5-feature, and 7-feature datasets. An 80/20 stratified train-test split was performed using a fixed random seed of 42 to ensure reproducibility. The same seed was also employed for the Decision Tree model, while the proposed ANN model was trained under a deterministic TensorFlow/Keras configuration by fixing the random seed to 42 and enabling deterministic operations through tf.config.experimental.enable_op_determinism(). For the Decision Tree, the default hyperparameter configuration provided by the scikit-learn library was adopted to reduce unnecessary model complexity. The SVM classifier employed a second-degree polynomial kernel (C = 1, γ = "scale"), Logistic Regression was configured with a maximum of 200 iterations, and the KNN classifier used three nearest neighbours with distance weighting and the Euclidean distance metric. These configurations were maintained throughout all experiments to ensure a fair and reproducible comparison among the evaluated models. The corresponding confusion matrices are presented in Figure 7, where rows correspond to the evaluated classifiers and columns represent the different input datasets. The accuracy (Acc) achieved by each model is reported below the corresponding confusion matrix.

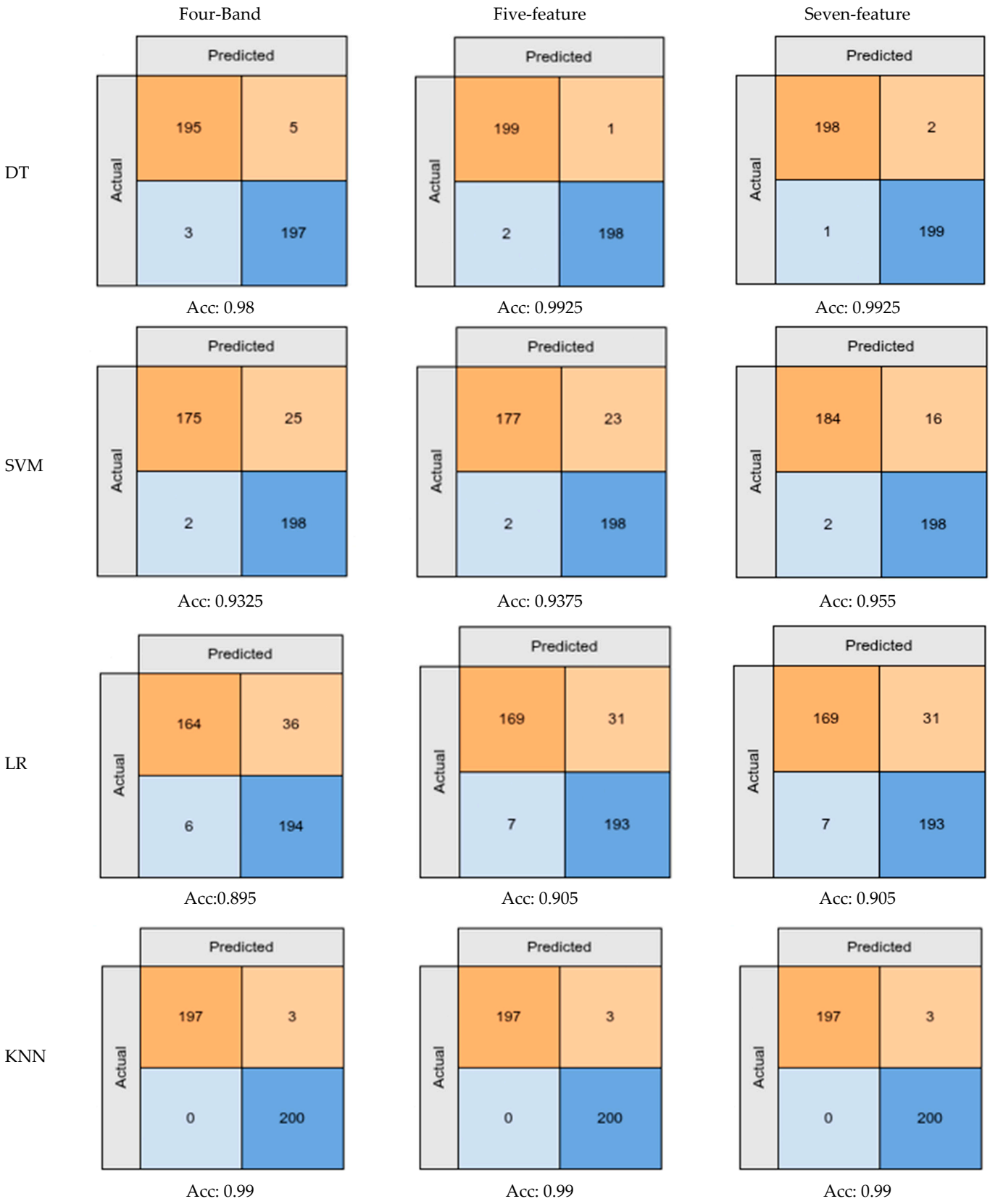


Figure 7. Confusion matrices obtained for the evaluated machine learning models using the 4-band, 5-feature, and 7-feature datasets.

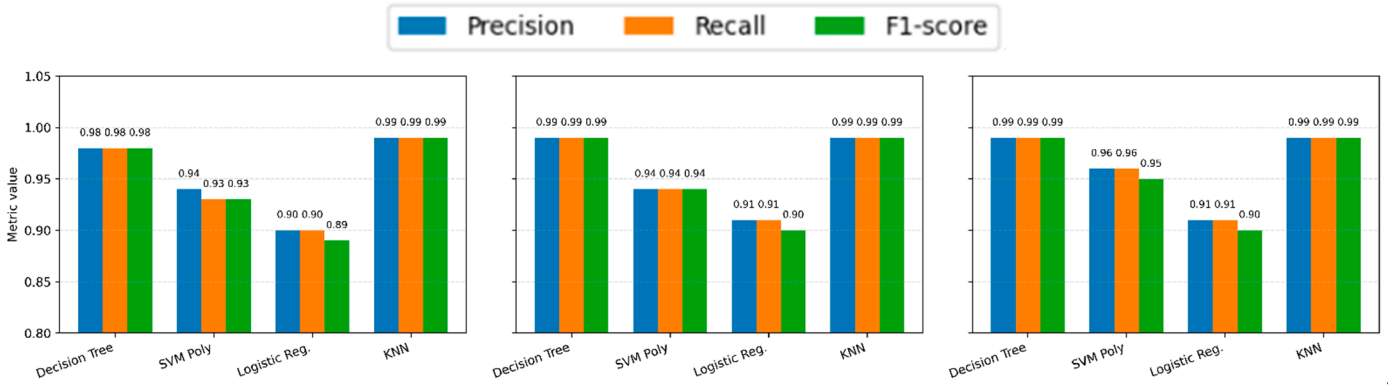
As shown in Figure 7, the KNN and Decision Tree (DT) classifiers consistently achieved the best performance across all three datasets, exhibiting the highest accuracies together with the lowest numbers of false-positive and false-negative classifications. For the original

4-band dataset (VNIR), KNN achieved an accuracy of 99.0%, while DT reached 98.0%. The inclusion of the NDVI feature slightly improved the DT performance, increasing its accuracy to 99.25%, whereas KNN maintained virtually identical performance. Similar behaviour was observed for the 7-feature dataset, indicating that both classifiers are robust to the incorporation of additional spectral features.

In contrast, Logistic Regression (LR) consistently produced the lowest classification performance regardless of the input dataset, with accuracies ranging from 89.5% to 90.5%. This behaviour suggests that linear decision boundaries are insufficient to adequately represent the spectral variability associated with asbestos–cement materials and the surrounding urban environment. The polynomial-kernel SVM exhibited intermediate performance for all datasets. Although its accuracy remained below that of KNN and DT, its performance improved progressively as additional features were incorporated, increasing from 93.25% for the 4-band dataset to 95.5% for the 7-feature dataset. This improvement indicates that the NDVI and, particularly, the PCA-derived features provide complementary information that enhances the discriminative capability of the SVM classifier.

Overall, the comparative analysis in Figure 7 demonstrates that incorporating additional spectral descriptors has only a limited effect on the performance of the best-performing classifiers (KNN and DT), which already achieve excellent results using the original multispectral bands. However, these additional features substantially benefit SVM by improving its classification accuracy and reducing misclassification errors. These findings suggest that non-parametric and tree-based approaches remain the most effective methods for asbestos–cement discrimination, while PCA-derived features provide complementary information that is particularly valuable for classifiers with more complex decision boundaries.

To provide a more comprehensive assessment of the classification performance of the four machine learning models, additional evaluation metrics, including Precision, Recall, and F1-score, were computed for the 4-band, 5-feature, and 7-feature datasets. These metrics complement overall accuracy by explicitly accounting for both false-positive and false-negative classifications. The corresponding results are summarized in Figure 8, where the performance of each classifier can be directly compared across the three evaluated datasets.



(**a**) (**b**) (**c**)

Figure 8. Comparison of precision, recall, and F1-score obtained by the evaluated machine learning models using the 4-band, 5-feature, and 7-feature datasets. Panels (**a**–**c**) correspond to the 4-band, 5-feature, and 7-feature datasets, respectively.

As shown in Figure 8, the KNN and Decision Tree (DT) classifiers consistently achieved the highest Precision, Recall, and F1-score values across all three datasets, confirming their robustness for asbestos–cement detection. Their performance remained consistently close to perfection, with F1-scores of approximately 0.99, regardless of the feature set employed.

The incorporation of the NDVI feature produced only marginal improvements, while the addition of the PCA-derived features maintained this excellent performance, indicating that the original multispectral information was already highly discriminative for these two classifiers.

The polynomial-kernel SVM exhibited the greatest improvement following feature augmentation. Precision, Recall, and F1-score progressively improved from the 4-band dataset to the 7-feature dataset, indicating that the NDVI and PCA-derived features provide complementary information that enhances the classifier's ability to discriminate asbestos–cement roofs from other surface materials.

In contrast, Logistic Regression consistently produced the lowest Precision, Recall, and F1-score values, although a slight improvement was also observed after incorporating the additional features. Nevertheless, its performance remained below that of the other evaluated classifiers, suggesting that linear decision boundaries are insufficient to adequately represent the spectral complexity of heterogeneous urban environments.

The comparative analysis demonstrates that incorporating NDVI and PCA-derived features provides only marginal benefits for the best-performing classifiers (KNN and DT), whereas it substantially improves the performance of SVM. These findings indicate that the original four-band VNIR data already contain sufficient discriminatory information for non-parametric and tree-based classifiers, while the additional features are particularly valuable for classifiers with more complex decision boundaries.

In addition to the conventional machine learning models, a compact feedforward artificial neural network (ANN) was designed to evaluate the potential of deep learning techniques for asbestos–cement detection. The ANN architecture was kept consistent across the three datasets, differing only in the number of input neurons to match the dimensionality of each dataset. Accordingly, the network received 4, 5, and 7 input features for the 4-band, 5-feature, and 7-feature datasets, respectively. These input features were connected to three fully connected hidden layers containing 16, 8, and 4 neurons, respectively, while the hidden layer architecture and the remaining training configuration were kept unchanged across all experiments. All hidden layers employed the ReLU (Rectified Linear Unit) activation function and incorporated L2 regularization to reduce the risk of overfitting. To further enhance model generalization, Dropout layers with a dropout rate of 20% were inserted after the first two hidden layers, randomly deactivating a subset of neurons during training. This strategy helps prevent excessive dependence on specific neurons and improves the network's ability to generalize to unseen data. The output layer comprised a single neuron with a sigmoid activation function, making it suitable for the binary classification task considered in this study. A standard decision threshold of 0.5 was used for binary classification, without further threshold optimization. The model was trained using the Adam optimizer with a learning rate of 0.001, while the binary cross-entropy loss function was employed to optimize the network parameters during training. The overall architecture of the proposed artificial neural network is illustrated in Figure 9.

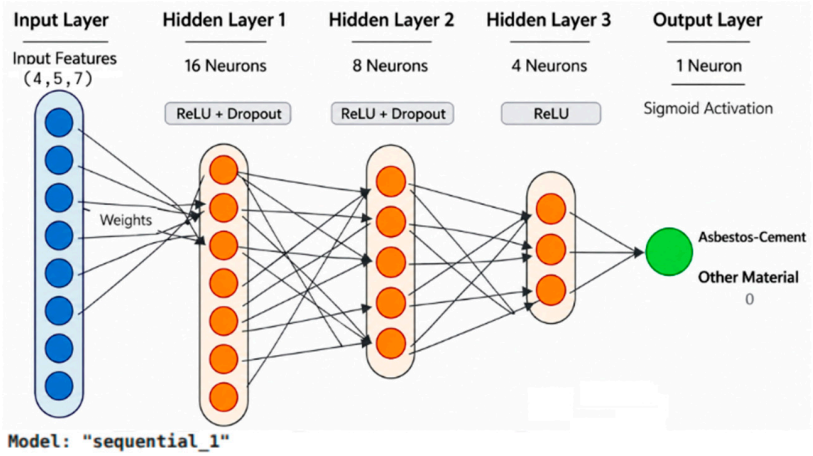
Based on Figure 9, the ANN was trained and evaluated using the 4-band, 5-feature, and 7-feature datasets over 100 training epochs. Figure 10 compares the corresponding training and validation accuracy and loss curves obtained for the three datasets.

As shown in Figure 10, the ANN exhibited stable learning behaviour for all three datasets, with progressively decreasing training and validation losses and classification accuracies approaching unity. However, noticeable differences in convergence dynamics emerged as additional features were incorporated.

The network trained on the original 4-band dataset achieved satisfactory convergence, although slightly greater variability was observed during the final training epochs. The inclusion of the NDVI feature resulted in smoother learning curves and earlier stabilization,

indicating a modest improvement in training stability. The most stable behaviour was obtained using the 7-feature dataset, where the incorporation of the PCA-derived components promoted faster convergence, reduced epoch-to-epoch variability, and improved agreement between the training and validation curves.

Overall, these results indicate that the additional spectral descriptors have a limited effect on the final predictive performance of the ANN but contribute significantly to improving training stability and convergence behaviour. In particular, the PCA-derived features facilitate the optimization process by providing complementary information that enhances feature representation during learning.



Model: "sequential_1"

Layer (type)	Output Shape	Param #
dense_4 (Dense)	(None, 16)	128
dropout_2 (Dropout)	(None, 16)	0
dense_5 (Dense)	(None, 8)	136
dropout_3 (Dropout)	(None, 8)	0
dense_6 (Dense)	(None, 4)	36
dense_7 (Dense)	(None, 1)	5

Total params: 305 (1.19 KB)
Trainable params: 305 (1.19 KB)
Non-trainable params: 0 (0.00 B)

Figure 9. Architecture of the artificial neural network model.

(**a**) 4-band

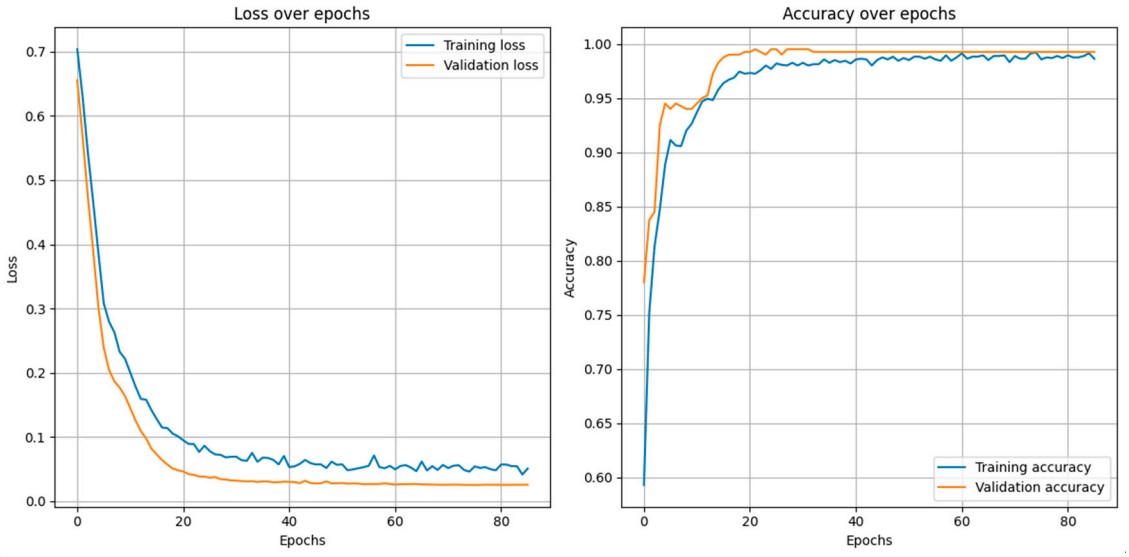


Figure 10. *Cont.*

(**b**) 5-feature

(**c**) 7-feature

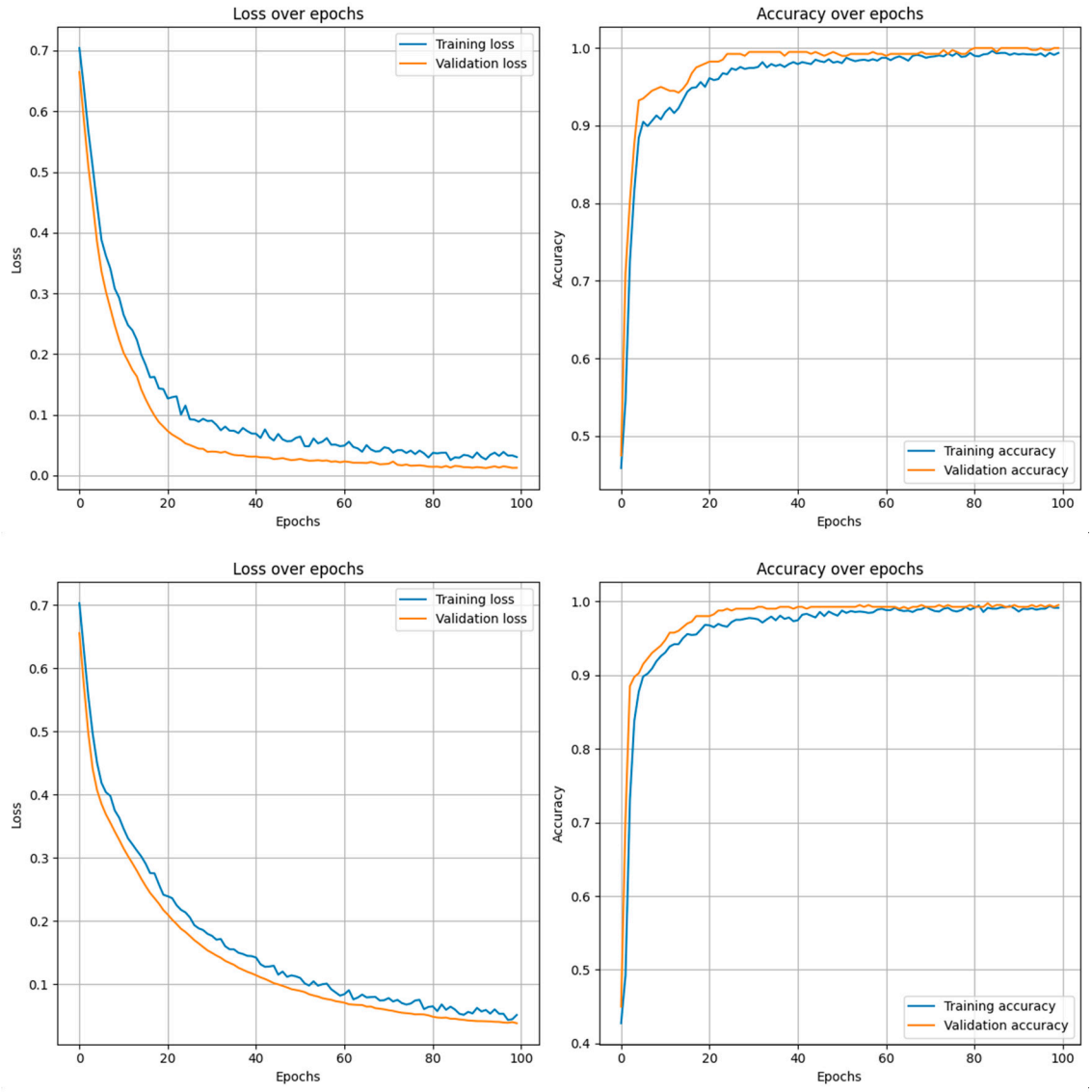


Figure 10. Training and validation accuracy and loss curves of the artificial neural network model for the 4-band, 5-feature, and 7-feature datasets. Panels (**a**–**c**) correspond to the 4-band, 5-feature, and 7-feature datasets, respectively.

3.3. Results of Phase 4: Model Deployment

Finally, the five trained classification models were deployed over the entire four-band reference image to perform pixel-level asbestos–cement detection. The resulting classification maps are presented in Figure 11, together with the percentage of the total image area classified as asbestos–cement by each model and the corresponding spatial distribution of the detected areas. The percentage displayed above each image represents the proportion of pixels classified as asbestos–cement relative to the total number of pixels in the study area. These results enable both quantitative and qualitative comparisons of the detection capabilities of the evaluated classification approaches.

According to the results presented in Figure 11, the KNN and artificial neural network (ANN) models exhibited the lowest classification error rates when applied to the original four-band dataset. Among these two approaches, the ANN model produced a more refined and spatially coherent detection pattern, which is reflected in the identification of 9.93% of the image pixels as asbestos–cement, compared with 14.28% detected by the KNN model. Visual inspection of the classification maps suggests that the ANN model generated fewer false-positive detections, resulting in a more selective identification of asbestos–cement roof

areas. In contrast, the KNN model, although highly accurate according to the quantitative metrics, classified a larger proportion of image pixels as asbestos–cement, indicating a greater tendency toward over-detection.

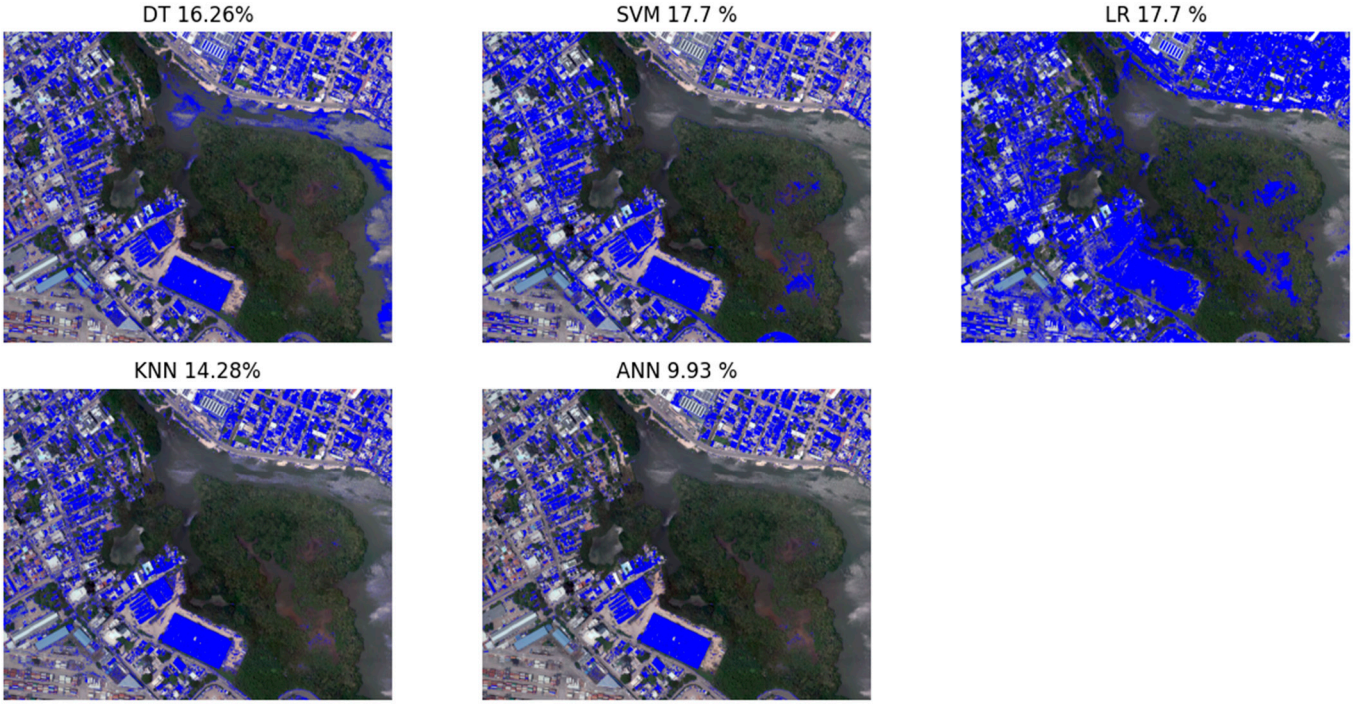


Figure 11. Classification results of the evaluated models on the original dataset. The percentage shown above each image corresponds to the area classified as asbestos–cement, expressed as a percentage (%) of the total image area.

The poorest classification performance was observed for the Logistic Regression model. As evidenced in Figure 11, this classifier incorrectly labelled several pixels associated with water bodies, vegetation, and road surfaces as asbestos–cement, resulting in a substantial number of false-positive detections. This behaviour highlights the limitations of linear classification methods for capturing the spectral complexity of heterogeneous urban environments in VNIR multispectral imagery.

The resulting classification maps are presented in Figure 12, together with the percentage of the total image area classified as asbestos–cement by each model and the corresponding spatial distribution of the detected areas. These results enable a visual and quantitative comparison of the influence of the additional NDVI feature on asbestos–cement detection performance.

The deployment results obtained using the five-feature dataset (Figure 12) were consistent with those observed for the original four-band dataset, with ANN producing the most spatially coherent detection maps and KNN showing a slight tendency toward over-detection. It is noteworthy that the two best-performing models, KNN and ANN, identified similar proportions of asbestos–cement pixels in both the four-feature and five-feature datasets. This finding suggests that the incorporation of the NDVI feature produced only a modest effect on the final spatial extent of the detected asbestos–cement areas, despite contributing to slight improvements in the quantitative classification metrics.

The resulting classification maps are presented in Figure 13, together with the percentage of the total image area classified as asbestos–cement by each model and the corresponding spatial distribution of the detected areas. These results provide a comprehensive basis

for evaluating the impact of the additional NDVI and PCA-derived features on full-image asbestos–cement detection.

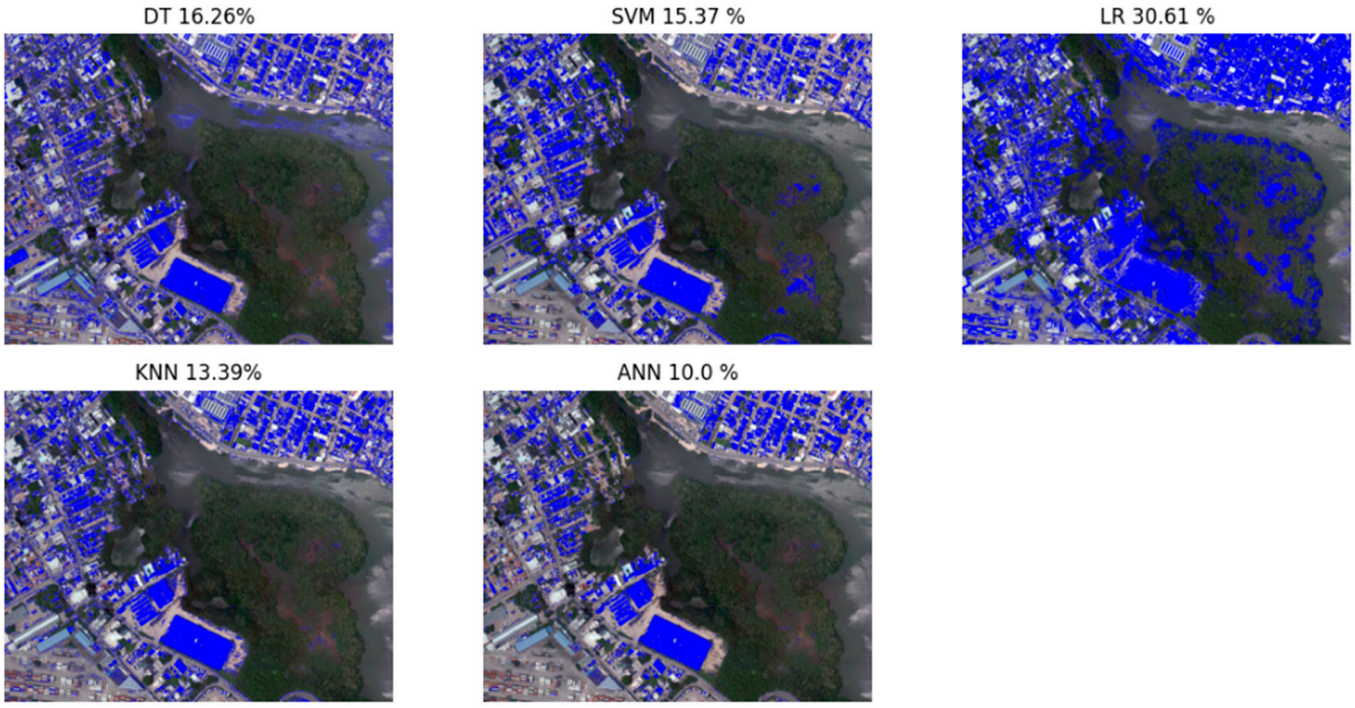


Figure 12. Results of model deployment on the complete image. The percentage shown above each image corresponds to the area classified as asbestos–cement, expressed as a percentage (%) of the total image area.

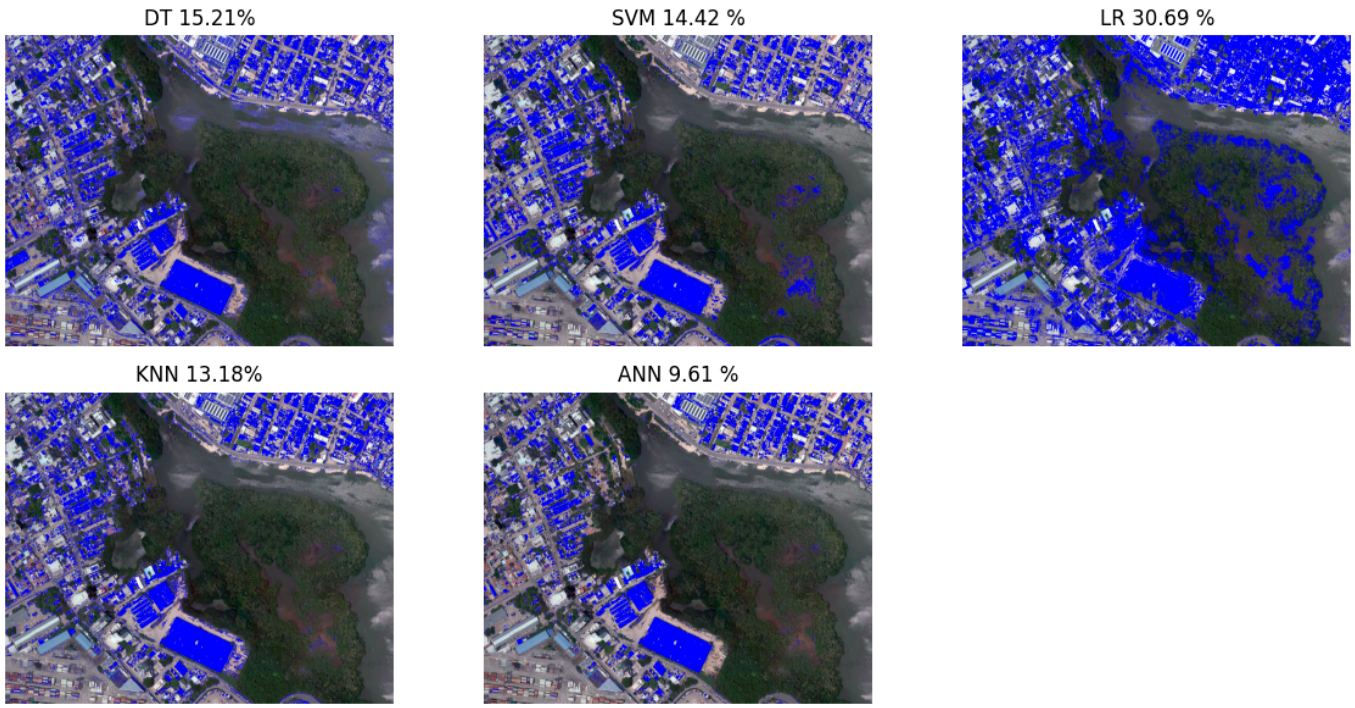


Figure 13. Full-image classification results obtained using the seven-feature dataset. The percentage shown above each image corresponds to the area classified as asbestos–cement, expressed as a percentage (%) of the total image area.

According to the results presented in Figure 13, the KNN and ANN models once again exhibited the lowest classification error rates, consistent with the results obtained using the

four-feature and five-feature datasets. Among these two approaches, the ANN model again produced the most refined and spatially coherent detection pattern, identifying 9.61% of the image pixels as asbestos–cement, compared with 13.18% detected by the KNN model. As observed in previous experiments, the ANN model generated fewer apparent false-positive detections, resulting in a more selective classification of asbestos–cement roof areas. In contrast, Logistic Regression continued to exhibit the weakest classification performance, frequently misclassifying pixels associated with water bodies, vegetation, and road surfaces as asbestos–cement. This behaviour remained consistent across all evaluated datasets and highlights the limitations of linear classification approaches for analyzing complex urban multispectral imagery.

Furthermore, the two best-performing models, KNN and ANN, detected comparable proportions of asbestos–cement pixels across the four-feature, five-feature, and seven-feature datasets. This finding suggests that, although the inclusion of NDVI and PCA-derived features contributed to improvements in several performance metrics, the overall spatial extent of the detected asbestos–cement areas remained relatively stable for the most effective classification approaches.

As a complement to the validation results presented previously, a comparison was conducted between the characteristic spectral signature, defined as the mean spectral signature of the asbestos cement sample signatures, and the mean spectral signature of the pixels classified by the three models that achieved the best results based on visual inspection for the dataset including the additional NDVI band and the two PCA bands. This comparison was performed considering that, in the domain of multispectral and hyperspectral imagery, the spectral signature is a distinctive indicator of the physical and chemical properties of materials. In this way, Figure 14 presents a graph showing the mean spectral signatures of the pixels classified by the decision tree, KNN, and the proposed ANN models on the seven band dataset, in comparison with the mean spectral signature corresponding to the same dataset.

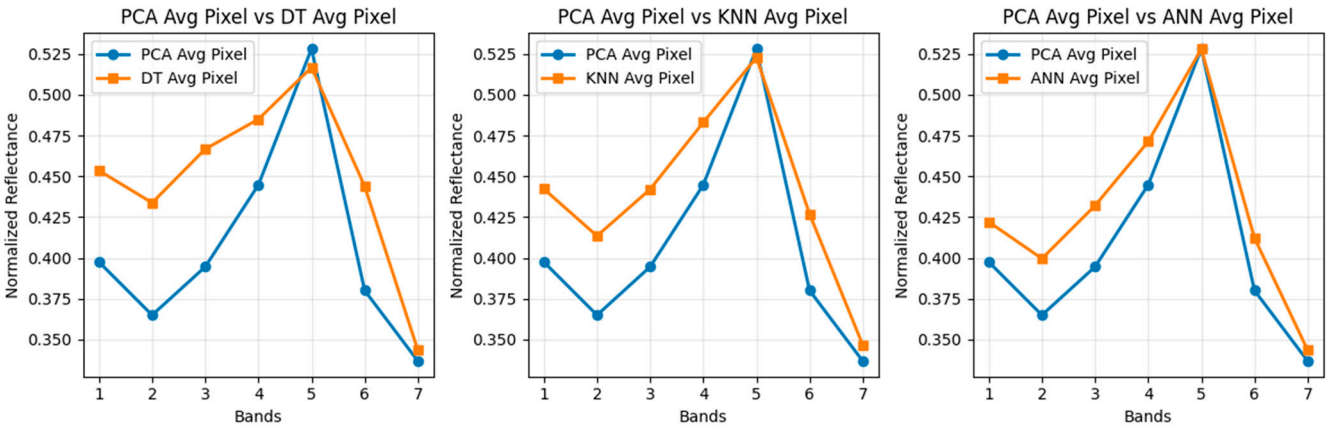


Figure 14. Comparison of the mean spectral signature of the sample pixels with the spectral signatures of the pixels classified by the DT, KNN, and ANN models.

According to the results presented in Figure 14, it can be observed that although all three models preserve the overall trend of the mean spectral signature, demonstrating similar behaviour in the distribution of reflectance across the seven bands, the ANN model exhibits the highest degree of agreement. Specifically, the mean signature obtained by this model more accurately reproduces both the progressive increase in reflectance up to the maximum at the fifth band and the subsequent decrease in the sixth and seventh bands, which is reflected in a smaller visual separation between the two curves throughout the entire spectrum. On the other hand, the decision tree and KNN models exhibit more

pronounced deviations, particularly in the first four bands, where they tend to overestimate reflectance values relative to the mean spectral signature. Thus, these results suggest that the ANN model preserves the spectral characteristics of the classified pixels more faithfully, providing additional evidence of its ability to identify more representative patterns within the dataset.

From a broader perspective, the present study contributes to the growing body of evidence demonstrating that accurate asbestos–cement detection can be achieved using low-dimensional VNIR multispectral imagery combined with lightweight machine learning approaches. In particular, the comparative evaluation of conventional machine learning algorithms and a compact feedforward artificial neural network across different feature-space configurations provides insight into the role of feature augmentation strategies such as NDVI and PCA in reduced-spectral-information scenarios. The results indicate that high detection accuracies can be achieved without relying on hyperspectral imagery or computationally intensive deep learning architectures, highlighting the potential of cost-effective multispectral solutions for operational environmental monitoring applications.

One of the most relevant findings of this study is that the proposed ANN consistently achieved outstanding classification performance across all experimental scenarios, comparable to that obtained by the Decision Tree and KNN models. However, when deployed over the complete image, the ANN produced the most refined detection results, particularly when trained on the seven-feature dataset, identifying 9.61% of the image pixels as asbestos–cement while exhibiting the lowest apparent level of classification errors in the visual analysis. These findings represent a relevant contribution to the remote sensing domain, particularly in applications where hyperspectral imagery may be impractical due to the substantial memory and computational requirements associated with the processing of large and highly redundant datasets [14–16]. The results demonstrate that highly accurate asbestos–cement detection can be achieved using a substantially smaller set of spectral features while maintaining superior computational efficiency. Consequently, the proposed methodology constitutes a promising alternative for real-time environmental monitoring applications, where the processing demands of hyperspectral imagery often limit operational implementation.

Another important contribution of this work is the exclusive use of open-source technologies throughout the entire workflow. The methodology was implemented using widely adopted Python libraries, including Rasterio, Spectral Python, Pandas, NumPy, Scikit-learn, and TensorFlow, all of which proved effective for asbestos–cement detection in VNIR multispectral imagery. This approach contrasts with previous studies, such as those reported by [25,26], which relied on proprietary software platforms such as ENVI for spectral image analysis. The use of open-source tools facilitates the customization and integration of different detection strategies while improving accessibility for research institutions and universities, particularly in developing countries where access to commercial software may be limited.

Despite the promising results obtained, some limitations should be considered when extrapolating the proposed methodology to other environmental monitoring contexts. Although the incorporation of NDVI and PCA-derived features improved classification performance and enhanced the detection capability of the proposed ANN model, the generation of these additional variables requires a preprocessing stage prior to model training and deployment. Nevertheless, this additional computational effort does not substantially affect the overall efficiency of the methodology because these operations are performed only once before model training, evaluation, and inference. Therefore, the primary benefit of incorporating these derived features is a more refined and reliable detection capability without introducing a significant computational burden during operational deployment.

Finally, the transition from four to five and seven features revealed a progressive improvement in classification performance and ANN training stability. The inclusion of NDVI produced modest but consistent gains across all classifiers, whereas the incorporation of PCA-derived components further improved convergence behaviour and spatial coherence in the ANN predictions. Nevertheless, the results indicate that high asbestos–cement detection accuracies can already be achieved using the original four-band NIR imagery, highlighting the potential of low-dimensional multispectral data for operational monitoring applications.

3.4. Discussion

The results obtained in this study demonstrate that asbestos–cement detection can be successfully performed using low-dimensional multispectral imagery combined with lightweight machine learning and neural network approaches. Although the evaluated datasets contained only four to seven spectral features, the proposed framework consistently achieved high classification performance across all experimental scenarios. This finding suggests that, for the specific task of asbestos–cement roof identification, classification performance depends not only on spectral dimensionality but also on the combination of spatial resolution, feature engineering strategies, and classifier selection.

One of the most relevant observations emerging from the experiments is the robustness of non-parametric classifiers, particularly KNN, across all feature configurations. The consistently high performance of KNN indicates that asbestos–cement roofs occupy a relatively well-defined region of the feature space when very high spatial resolution imagery is employed. Similarly, the ANN demonstrated remarkable stability throughout the experiments, producing not only excellent quantitative metrics but also more spatially coherent detection maps after deployment over the complete image. This behaviour suggests that the neural network was capable of capturing more generalized spectral relationships while reducing the over-detection tendencies occasionally observed in nearest-neighbour approaches.

Although NDVI and PCA do not introduce new physical information, they provide alternative representations of the original spectral information that enhance its discriminative capacity. Specifically, NDVI emphasizes the spectral contrast associated with vegetation, facilitating its separation from asbestos–cement roofs, while PCA concentrates most of the data variance into a reduced set of components, minimizing redundancy among the original bands and reducing the influence of noise. Consequently, these transformed features provide the classifier with a more informative feature space, improving class separability. In the experiments conducted, the progressive incorporation of NDVI and PCA-derived components produced modest but systematic improvements in classification performance and ANN convergence behaviour. Although the gains observed in the quantitative metrics were relatively small, the additional feature representations contributed to greater model stability and improved map interpretability. These findings highlight the value of incorporating physically and statistically meaningful derived features, which can enhance the discriminative capability of multispectral imagery while avoiding the substantially higher dimensionality and computational cost typically associated with hyperspectral data. This result suggests that carefully selected feature engineering strategies can partially compensate for reduced spectral dimensionality without requiring additional sensors or more complex acquisition systems.

The progressive incorporation of NDVI and PCA-derived components produced modest but systematic improvements in classification performance and ANN convergence behaviour. Although the gains observed in the quantitative metrics were relatively small, the additional features contributed complementary information that improved model stability and map interpretability. This result highlights an important practical consider-

ation in multispectral image analysis: feature engineering can partially compensate for reduced spectral dimensionality without requiring additional sensors or more complex acquisition systems.

The findings of the present study are consistent with a growing body of literature demonstrating that accurate asbestos detection does not necessarily require hyperspectral imagery. Recent work based on WorldView-3 VNIR imagery reported F1-scores exceeding 97% using lightweight machine learning approaches, with KNN-based methods emerging as particularly effective classifiers for asbestos–cement discrimination in urban environments. The strong performance of KNN observed in the present study, therefore, reinforces previous evidence supporting the suitability of neighbourhood-based classifiers for asbestos roof detection under limited spectral dimensionality conditions [34].

Similarly, convolutional neural network approaches developed using RGB and colour-infrared aerial imagery in Poland achieved overall accuracies between 87% and 89% for asbestos roof identification. Although CNNs benefit from their ability to incorporate spatial context and roof morphology, the results obtained in the present work suggest that very high classification accuracies can also be achieved using considerably simpler architectures and substantially smaller training datasets when high-spatial-resolution multispectral imagery is available. This observation may be particularly relevant for institutions lacking access to large annotated databases or high-performance computing resources [29].

Several studies based on hyperspectral imagery have reported excellent results for asbestos mapping over large territories, including regional-scale applications involving hundreds of spectral bands and thousands of square kilometres. These investigations benefit from the mineralogical absorption features available in hyperspectral data and are particularly valuable for large-scale inventory generation. However, such approaches often involve considerable data volumes, more complex preprocessing stages, and greater computational requirements. The present study does not aim to replace hyperspectral methodologies but rather to demonstrate that operational asbestos screening can also be performed using lower-dimensional multispectral datasets when combined with appropriate machine learning strategies [35].

The importance of ground truth quality repeatedly emerges throughout the asbestos remote sensing literature and constitutes one of the principal factors governing model performance. Large-scale studies conducted in Taiwan highlighted the necessity of extensive and geographically representative training databases to ensure transferability across broad territories. Similarly, studies conducted in Poland reported the need for municipality-specific calibration datasets to maintain classification accuracy under changing environmental conditions. The present investigation relied on field-verified asbestos roofs for the positive class, which increased confidence in the reference data used during model development. Nevertheless, extending the methodology to additional cities and climatic conditions will require further validation efforts and expanded reference datasets [29,36].

Several limitations should also be acknowledged. First, the analysis was conducted using imagery acquired over a single urban sector and under a single acquisition date. Consequently, the effects of seasonal variability, roof ageing, weathering processes, and illumination conditions remain outside the scope of the present investigation. Second, the methodology relies on pixel-based classification and therefore does not explicitly exploit roof geometry, texture information, or neighbourhood context. The incorporation of object-based approaches or hybrid pixel-object frameworks could potentially improve discrimination among spectrally similar urban materials. Finally, the use of randomly selected pixels may introduce some degree of spatial dependence between training and testing samples, potentially leading to optimistic estimates of predictive performance.

From an operational perspective, the proposed methodology offers several advantages for environmental monitoring applications. The use of open-source software, lightweight machine learning models, and low-dimensional multispectral imagery substantially reduces technical and economic barriers to implementation. Such characteristics are particularly relevant for developing countries, where legacy asbestos infrastructure remains widespread while access to hyperspectral imagery and advanced computing facilities is often limited. Under these circumstances, the proposed framework may constitute a practical support tool for prioritizing inspection campaigns, planning remediation programmes, and supporting evidence-based asbestos management strategies [34,37].

4. Conclusions

This study investigated the effectiveness of conventional machine learning algorithms and a sequential artificial neural network (ANN) for asbestos–cement detection using VNIR multispectral imagery with different feature configurations. To this end, three datasets were evaluated, including the original four-band dataset and two enhanced datasets incorporating NDVI and PCA-derived features. The results demonstrated that the KNN and ANN models consistently achieved the highest classification performance across all experimental scenarios. Although the Decision Tree model produced metrics comparable to those of KNN, its deployment over complete images revealed a greater number of visually identifiable classification errors. In contrast, the ANN generated the most refined and spatially coherent asbestos–cement detection maps, highlighting the potential of combining feature-enhanced multispectral datasets with deep learning techniques for material identification tasks.

Among the evaluated approaches, the proposed ANN architecture, consisting of three hidden layers with 16, 8, and 4 neurons, exhibited the most stable learning behaviour and the most consistent performance throughout the experiments. The best results were obtained using the seven-feature dataset, which combined the original VNIR bands with NDVI and PCA-derived features. Unlike the other models, whose performance stabilized after approximately 20 epochs, the ANN displayed stable convergence from the early stages of training, indicating a robust and efficient learning process.

The incorporation of PCA-derived components proved particularly beneficial for the ANN model, enhancing training stability, accelerating convergence, and providing complementary discriminative information for asbestos–cement identification. Consequently, the seven-feature configuration achieved slightly superior performance across both quantitative evaluation metrics and visual interpretation of the classification maps.

The findings also demonstrate that accurate asbestos–cement detection can be achieved using multispectral imagery and open-source technologies, reducing the computational burden typically associated with hyperspectral image analysis while maintaining a high level of classification performance. The successful integration of Rasterio, Spectral Python, Pandas, NumPy, Scikit-learn, and TensorFlow confirms the feasibility of developing cost-effective and reproducible workflows for remote sensing applications.

Therefore, the proposed framework may serve as a reference for research institutions and universities seeking to implement material detection methodologies based on multispectral imagery. Beyond the reported classification accuracies, this study contributes to the growing body of research exploring lightweight and operational remote sensing solutions for material detection in urban environments.

Future research should focus on evaluating the proposed ANN model using additional image sources, particularly satellite imagery, to assess its generalization capability across different spatial and spectral resolutions. Furthermore, the inclusion of alternative spectral

indices and dimensionality reduction techniques should be investigated to determine their potential contribution to improving classification performance and detection accuracy.

Author Contributions: Conceptualization, G.E.C.-G. and M.A.O.-A.; methodology, G.E.C.-G., I.E.C.F., and M.A.O.-A.; software, G.E.C.-G. and I.E.C.F.; validation, G.E.C.-G., I.E.C.F., J.E.M.M., M.S., and M.A.O.-A.; formal analysis, G.E.C.-G., M.S., and M.A.O.-A.; investigation, G.E.C.-G., I.E.C.F., J.E.M.M., and M.A.O.-A.; resources, M.S. and M.A.O.-A.; data curation, G.E.C.-G. and I.E.C.F.; writing—original draft preparation, G.E.C.-G.; writing—review and editing, G.E.C.-G., I.E.C.F., J.E.M.M., M.S., and M.A.O.-A.; visualization, G.E.C.-G. and I.E.C.F.; supervision, M.S. and M.A.O.-A.; project administration, M.S. and M.A.O.-A.; funding acquisition, M.S. All authors have read and agreed to the published version of the manuscript.

Funding: This research was funded by the General System of Royalties of Colombia (SGR) under project code BPIN 2020000100366.

Institutional Review Board Statement: Not applicable.

Informed Consent Statement: Not applicable.

Data Availability Statement: The original contributions presented in this study are included in the article. Further inquiries can be directed to the corresponding author.

Acknowledgments: This article represents a deliverable within the project "Formulation of an integral strategy to reduce the impact on public and environmental health due to the presence of asbestos in the territory of the Department of Bolivar," financially supported by the General System of Royalties of Colombia (SGR) under project code BPIN 2020000100366. This project was a collaboration between the University of Cartagena, Colombia and the Asbestos-Free Colombia Foundation. The authors acknowledge Carlos Castrillón, Mario Salom, Liseth Sequeda, Federico Frassy, David Valdelamar-Martínez, Michelle Cecilia Montero Acosta, Margareth Peña Castro, and the research group for their efforts.

Conflicts of Interest: The authors declare no conflicts of interest.

References

1. Torres Gil, L.K.; Valdelamar Martínez, D.; Saba, M. The Widespread Use of Remote Sensing in Asbestos, Vegetation, Oil and Gas, and Geology Applications. *Atmosphere* **2023**, *14*, 172. [CrossRef]
2. Abdulraheem, M.I.; Zhang, W.; Li, S.; Moshayedi, A.J.; Farooque, A.A.; Hu, J. Advancement of Remote Sensing for Soil Measurements and Applications: A Comprehensive Review. *Sustainability* **2023**, *15*, 15444. [CrossRef]
3. Awange, J.; Kiema, J. Fundamentals of Remote Sensing. In *Environmental Science and Engineering*; Springer: Cham, Switzerland, 2019; pp. 115–123.
4. Benediktsson, J.A.; Wu, Z. Distributed Computing for Remotely Sensed Data Processing [Scanning the Section]. *Proc. IEEE* **2021**, *109*, 1278–1281. [CrossRef]
5. Fu, W.; Ma, J.; Chen, P.; Chen, F. Remote Sensing Satellites for Digital Earth. In *Manual of Digital Earth*; Springer: Singapore, 2020; pp. 55–123.
6. Joshi, N.; Baumann, M.; Ehammer, A.; Fensholt, R.; Grogan, K.; Hostert, P.; Jepsen, M.; Kuemmerle, T.; Meyfroidt, P.; Mitchard, E.; et al. A Review of the Application of Optical and Radar Remote Sensing Data Fusion to Land Use Mapping and Monitoring. *Remote Sens.* **2016**, *8*, 70. [CrossRef]
7. Wang, Z.; Ma, Y.; Zhang, Y.; Shang, J. Review of Remote Sensing Applications in Grassland Monitoring. *Remote Sens.* **2022**, *14*, 2903. [CrossRef]
8. Yao, H.; Qin, R.; Chen, X. Unmanned Aerial Vehicle for Remote Sensing Applications—A Review. *Remote Sens.* **2019**, *11*, 1443. [CrossRef]
9. Cheng, M.-F.; Mukundan, A.; Karmakar, R.; Valappil, M.A.E.; Jouhar, J.; Wang, H.-C. Modern Trends and Recent Applications of Hyperspectral Imaging: A Review. *Technologies* **2025**, *13*, 170. [CrossRef]
10. Composto, A.; Privitera, L.; Riva, M.; Ardini, B.; Manzoni, C.; Riva, M.; Aquilina, K.; Valentini, G.; Giuliani, S. Hyperspectral Imaging for Tumor Resection Guidance in Surgery: A Systematic Review of Preclinical and Clinical Studies. *J. Biomed. Opt.* **2025**, *30*, S23909. [CrossRef] [PubMed]
11. Nalepa, J. Recent Advances in Multi- and Hyperspectral Image Analysis. *Sensors* **2021**, *21*, 6002. [CrossRef] [PubMed]

12. Rodriguez-Pulido, F.J.; González-Miret, M.L.; Heredia, F.J. Application of Imaging Techniques for the Evaluation of Phenolic Maturity of Grape Seeds. *Opt. Pura Y Apl.* **2017**, *50*, 1–11. [CrossRef]
13. Hernandez-Valdez, J.E.; Castro-Salinas, D.; Honorio-Javes, C.E.; Pajuelo-Risco, F.M. In Ovo Sexing with Hyperspectral Imaging (HSI): A Nondestructive and Non-Invasive Method. *Agroindustrial Sci.* **2024**, *13*, 189–198. [CrossRef]
14. Fang, Q.; Wang, Z.; Wang, J.; Zhang, L. ARM-Net: A Tri-Phase Integrated Network for Hyperspectral Image Compression. *Sensors* **2025**, *25*, 1843. [CrossRef] [PubMed]
15. Paoletti, M.E.; Haut, J.M.; Pereira, N.S.; Plaza, J.; Plaza, A. Ghostnet for Hyperspectral Image Classification. *IEEE Trans. Geosci. Remote Sens.* **2021**, *59*, 10378–10393. [CrossRef]
16. Zhang, J.; Su, R.; Fu, Q.; Ren, W.; Heide, F.; Nie, Y. A Survey on Computational Spectral Reconstruction Methods from RGB to Hyperspectral Imaging. *Sci. Rep.* **2022**, *12*, 11905. [CrossRef] [PubMed]
17. Fernandez, D.; Gonzalez, C.; Mozos, D.; Lopez, S. FPGA Implementation of the Principal Component Analysis Algorithm for Dimensionality Reduction of Hyperspectral Images. *J. Real Time Image Process.* **2019**, *16*, 1395–1406. [CrossRef]
18. Islam, M.R.; Ahmed, B.; Hossain, M.A.; Uddin, M.P. Mutual Information-Driven Feature Reduction for Hyperspectral Image Classification. *Sensors* **2023**, *23*, 657. [CrossRef] [PubMed]
19. Liu, J.; Zhang, L.; Wang, J.; Qu, L. Lightweight Band-Adaptive Hyperspectral Image Compression with Feature Decouple and Recurrent Model. *IEEE J. Sel. Top. Appl. Earth Obs. Remote Sens.* **2025**, *18*, 16733–16749. [CrossRef]
20. Bian, L.; Suo, J.; Situ, G.; Li, Z.; Fan, J.; Chen, F.; Dai, Q. Multispectral Imaging Using a Single Bucket Detector. *Sci. Rep.* **2016**, *6*, 24752. [CrossRef] [PubMed]
21. Shi, Y.; Zhang, L.; Shu, X.; Zhang, K.; Yan, Y.; Yuan, W.; Yu, Y.; Gong, Y. Development of a Multispectral Imaging Apparatus for Cost-Effective Fundus Disease Detection. *Biomed. Opt. Express* **2025**, *16*, 2482. [CrossRef] [PubMed]
22. Zelinski, M.; Mastin, A.; Castillo, V.; Yoxall, B. Optimal Band Selection for Target Detection with a LWIR Multispectral Imager. *J. Appl. Remote Sens.* **2022**, *16*, 026505. [CrossRef]
23. Bonifazi, G.; Capobianco, G.; Serranti, S.; Malinconico, S.; Paglietti, F. Asbestos Detection in Construction and Demolition Waste Adopting Different Classification Approaches Based on Short Wave Infrared Hyperspectral Imaging. *Detritus* **2022**, *20*, 90–99. [CrossRef]
24. Bonifazi, G.; Capobianco, G.; Serranti, S. Asbestos Containing Materials Detection and Classification by the Use of Hyperspectral Imaging. *J. Hazard. Mater.* **2018**, *344*, 981–993. [CrossRef] [PubMed]
25. Bellagamba, S.; Malinconico, S.; Paglietti, F.; Bonifazi, G.; Serranti, S.; Aurigemma, A. Remote Sensing for Asbestos Roofing Mapping: Mantua Case Study Using WorldView-3 Images. *Spectrochim. Acta Part A Mol. Biomol. Spectrosc.* **2026**, *348*, 127160. [CrossRef] [PubMed]
26. Shepherd, J.E.; Sagi, E.; Zagron, G.; Ben-Dor, E. Detection of Asbestos-Based Cement Rooftops in Conflict-Affected Settings Using EnMAP Hyperspectral Data: A Research Article. *Sci. Rep.* **2025**, *15*, 24166. [CrossRef] [PubMed]
27. Jeong, Y.; Yu, J.; Wang, L.; Huynh, H.H.; Kim, H.-C. Monitoring Asbestos Mine Remediation Using Airborne Hyperspectral Imaging System: A Case Study of Jefferson Lake Mine, US. *Remote Sens.* **2022**, *14*, 5572. [CrossRef]
28. Hikuwai, M.; Patorniti, N.; Vieira, A.; Frangioudakis Khatib, G.; Stewart, R. Artificial Intelligence for the Detection of Asbestos Cement Roofing: An Investigation of Multi-Spectral Satellite Imagery and High-Resolution Aerial Imagery. *Sustainability* **2023**, *15*, 4276. [CrossRef]
29. Krówczyńska, M.; Raczko, E.; Staniszewska, N.; Wilk, E. Asbestos—Cement Roofing Identification Using Remote Sensing and Convolutional Neural Networks (CNNs). *Remote Sens.* **2020**, *12*, 408. [CrossRef]
30. Chimaobi, A.E.; Lu, Y. Using Convolutional Neural Network for Image Classification and Segmentation. *Comput. Eng. Intell. Syst.* **2022**, *13*, 21. [CrossRef]
31. Martinez-Plumed, F.; Contreras-Ochando, L.; Ferri, C.; Hernandez-Orallo, J.; Kull, M.; Lachiche, N.; Ramirez-Quintana, M.J.; Flach, P. CRISP-DM Twenty Years Later: From Data Mining Processes to Data Science Trajectories. *IEEE Trans. Knowl. Data Eng.* **2021**, *33*, 3048–3061. [CrossRef]
32. Razali, N.; Ismail, S.; Mustapha, A. Machine Learning Approach for Flood Risks Prediction. *IAES Int. J. Artif. Intell.* **2020**, *9*, 73. [CrossRef]
33. Saltz, J.S.; Krasteva, I. Current Approaches for Executing Big Data Science Projects—A Systematic Literature Review. *PeerJ Comput. Sci.* **2022**, *8*, e862. [CrossRef] [PubMed]
34. Saba, M.; Coronado-Hernández, O.E.; Bustillo-LeCompte, C. Satellite-Based Detection of Asbestos-Cement Roofs Using WorldView-3 VNIR Data: An Affordable Evaluation Tool for Sustainable Management of Hazardous Building Infrastructure. *J. Hazard. Mater.* **2026**, *508*, 141864. [CrossRef] [PubMed]
35. Gubiani, D.; Sgrazzutti, G.; Basso, M.; Viero, E.; Tavaris, D.; Foresti, G.L.; Scagnetto, I. A Dynamic Neural Network Model for the Identification of Asbestos Roofings in Hyperspectral Images Covering a Large Regional Area. *Comput. Civ. Infrastruct. Eng.* **2025**, *40*, 879–894. [CrossRef]

36. Yu, T.-T.; Lin, Y.-C.; Lan, S.-C.; Yang, Y.-E.; Wu, P.-Y.; Lin, J.-C. Mapping Asbestos-Cement Corrugated Roofing Tiles with Imagery Cube via Machine Learning in Taiwan. *Remote Sens.* **2022**, *14*, 3418. [CrossRef]
37. Bonifazi, G.; Aurigemma, A.; Salas-Cáceres, J.; Lorenzo-Navarro, J.; Serranti, S.; Paglietti, F.; Bellagamba, S.; Malinconico, S. A Python-Based Workflow for Asbestos Roof Mapping and Temporal Monitoring Using Satellite Imagery. *Geomatics* **2026**, *6*, 41. [CrossRef]

Disclaimer/Publisher's Note: The statements, opinions and data contained in all publications are solely those of the individual author(s) and contributor(s) and not of MDPI and/or the editor(s). MDPI and/or the editor(s) disclaim responsibility for any injury to people or property resulting from any ideas, methods, instructions or products referred to in the content.